



Single-phase $Gd_{0.2}La_{0.2}Ce_{0.2}Hf_{0.2}Zr_{0.2}O_2$ and $Gd_{0.2}La_{0.2}Y_{0.2}Hf_{0.2}Zr_{0.2}O_2$ nanoparticles as efficient photocatalysts for the reduction of Cr(VI) and degradation of methylene blue dye



Mariappan Anandkumar ^a, Ajay Lathe ^b, Anil M. Palve ^b, Atul Suresh Deshpande ^{a,*}

^a Department of Materials Science and Metallurgical Engineering, Indian Institute of Technology Hyderabad, Kandi, Sangareddy, 502285, India

^b Department of Chemistry, Mahatma Phule Arts, Science and Commerce College, Panvel, Navi-Mumbai, 410206, India

ARTICLE INFO

Article history:

Received 7 July 2020

Received in revised form

11 August 2020

Accepted 12 August 2020

Available online 17 August 2020

Keywords:

Equiatomic multicomponent oxide

Solid solution

Nanoparticles

Photocatalyst

Cr(VI) remediation

Methylene blue degradation

ABSTRACT

We report for the first time the use of noble metal-free multi-component equiatomic oxide as photocatalysts with excellent performance for natural sunlight driven degradation of Cr(VI) and methylene blue dye. The multi-component oxide nanoparticles with a composition $Gd_{0.2}La_{0.2}Ce_{0.2}Hf_{0.2}Zr_{0.2}O_2$ and $Gd_{0.2}La_{0.2}Y_{0.2}Hf_{0.2}Zr_{0.2}O_2$ were synthesized by simple co-precipitation followed by peptization in acid to obtain nanoparticle sol and calcined at 500 °C. The nanopowders were characterized by x-ray diffraction (XRD), UV–Visible spectroscopy (UV–Vis), and high-resolution transmission electron microscopy (HRTEM). The complete (~100%) reduction of Cr(VI) to Cr(III) was observed after 90 and 100 min for the calcined $Gd_{0.2}La_{0.2}Ce_{0.2}Hf_{0.2}Zr_{0.2}O_2$ and $Gd_{0.2}La_{0.2}Y_{0.2}Hf_{0.2}Zr_{0.2}O_2$ respectively, under exposure to natural sunlight. In addition, 70% degradation of methylene blue is observed in 180 min. The effective photocatalytic activity of multi-component oxides can be attributed to their unique composition containing five components in equimolar amounts. The role of oxygen vacancies in photocatalytic reduction of Cr(VI) and the degradation of methylene blue is also discussed.

© 2020 Elsevier B.V. All rights reserved.

1. Introduction

Contamination of natural drinking water as a result of toxic industrial waste discharge without appropriate treatment poses serious environmental and health hazards. For instance, industries such as dyeing, electroplating, mining, textile, paper, etc. are the major contributors for increasing hazardous pollutants. Organic contaminants such as methyl orange, methylene blue, and other dyes are toxic and non-biodegradable and remain as an environmental pollutant for long periods of time. In addition, heavy elements such as Cr, Pb, As, Hg, Cd, etc. are classified as the most prominent hazardous contaminants among other elements [1–4]. Chromium in wastewater discharge generally exists as both trivalent Cr(III) and hexavalent Cr(VI) ions. Cr(VI) is relatively more toxic as compared to Cr(III). The toxicity of Cr(VI) stems from its tendency to bind with various proteins and nucleic acids resulting in skin cancer and liver damage problems [4]. The Cr(III) species can be eliminated from wastewater by precipitating them in the form of

hydroxides. However, Cr(VI) cannot be eliminated by precipitation process owing to the fact that all Cr(VI) species are water-soluble. Thus, hexavalent chromium has been the cause of serious concern due to its toxicity and difficulty in its removal from water due to the high solubility of various Cr(VI) compounds.

To remediate the toxic Cr(VI) ions, different strategies have been followed, for example, ion-exchange process, membrane filtration, and the reduction of Cr(VI) to Cr(III). Among those, one of the most followed methods in converting noxious Cr(VI) to fairly innocuous Cr(III) is by using a chemical reduction method. The Cr(III) thus formed can be easily converted into precipitates as chromium hydroxides $Cr(OH)_3$ [4]. The photocatalytic reduction is a popular and well known green technique in converting potentially toxic Cr(VI) to less toxic Cr(III). The method involves irradiation of photons in the form of sunlight or visible light over a solution containing pollutant chemicals and nanoparticles. TiO_2 is one of the most widely used oxides as a photocatalyst material owing to its low toxicity, low cost, and photochemical stability [5,6]. Similarly, other oxides such as $Cu_2O/BiVO_4$ [7], ZnO [6,8,9], iron oxide [10], CeO_2 [11,12], ZrO_2 [13], etc., were also used as photocatalyst for the conversion of Cr(VI) to Cr(III).

A plethora of semiconductor materials, including oxides,

* Corresponding author.

E-mail address: atuldeshpande@msme.iith.ac.in (A.S. Deshpande).

chalcogenides, nitrides, have been explored as active materials for photocatalysis [14–20]. Literature reports show that for all these wide ranges of materials, there are several common properties which affect the photocatalytic activity such as bandgap, recombination rates, conduction band energy, and valence band energy. Accordingly, energy band engineering can be achieved by either doping an aliovalent element or adding another element as a composite [21]. In this way, the conduction band energy and valence band energy could be engineered, and thus the photocatalytic efficiency can be increased.

Additionally, defects in the crystal system can also play a role in the photocatalyst. Similar defect induced enhanced photocatalytic behavior has been reported for the CeO₂ system [22]. Apart from these conventional approaches to tailor functional properties, a new class of materials, namely multi-component oxides or high entropy oxides, have gained a lot of attention. Solid solutions or doped systems usually have a single principal component, which dictates the properties of the system. In contrast, for multi-component oxide systems, which comprise of five or more elements in nearly equiatomic compositions, the system behavior is collective and often synergistic, which subsequently leads to enhanced or sometimes unexpected functional behavior. There are many recent reports on the synthesis and applications of multi-component oxides in energy storage, catalysis, magnetic properties, optical properties, etc. [23–26].

Among all the reported high entropy oxides, we have reported the synthesis of single-phase Gd_{0.2}La_{0.2}Ce_{0.2}Hf_{0.2}Zr_{0.2}O₂ and Gd_{0.2}La_{0.2}Y_{0.2}Hf_{0.2}Zr_{0.2}O₂ multi-component oxide nanoparticles and we have studied the photoluminescent properties of Gd_{0.2}La_{0.2}Ce_{0.2}Hf_{0.2}Zr_{0.2}O₂ by Eu³⁺ doping [27,28]. Here, for the first time, we report the use of these two noble metal-free multi-component oxides as photocatalysts towards the reduction of Cr(VI) to Cr(III) and degradation of methylene blue (MB) dye. We have selected the above two multi-component oxides for photocatalytic studies based on the fact that all the individual oxides such as CeO₂, Gd₂O₃, HfO₂, La₂O₃, Y₂O₃, and ZrO₂ have been known to exhibit photocatalytic activities [11–13,29–35]. Both the single-phase compositions possess a large number of intrinsic oxygen vacancies due to the difference in the valence of individual elements. In addition, the synthesis method employed by us produces non-agglomerated nanoparticles with a particle size in the range of 3–5 nm. High surface-to-volume ratio due to such small particle sizes, can consequently lead to enhanced photocatalytic activity. We also propose the possible mechanism for photocatalytic detoxification of Cr(VI) as well as degradation of MB dye.

2. Experimental section

2.1. Materials

Gadolinium nitrate hydrate (Gd(NO₃)₃·H₂O, Alfa Aesar, 99.9%), lanthanum nitrate hexahydrate (La(NO₃)₃·6H₂O, Alfa Aesar, 99.9%), cerium ammonium nitrate (Ce(NH₄)₂(NO₃)₆, Sigma-Aldrich, 98.5%), yttrium nitrate hexahydrate (Y(NO₃)₃·6H₂O, Sigma-Aldrich, 99.8%), hafnium chloride (Cl₄Hf, Alfa Aesar, 98%), zirconyl chloride octahydrate (ZrOCl₂·8H₂O, Sigma-Aldrich, 98%), ammonia solution (NH₄OH, Merck, 25%), nitric acid (HNO₃, Merck, 69%), potassium dichromate (K₂Cr₂O₇, Sigma-Aldrich), methanol (CH₃OH, Sigma-Aldrich), and 100% GR formic acid (HCOOH, Merck India). Analytical grade reagents were used without further purification for the synthesis of multi-component oxides and photoreduction process.

2.1.1. Synthesis of Gd_{0.2}La_{0.2}Ce_{0.2}Hf_{0.2}Zr_{0.2}O₂ and Gd_{0.2}La_{0.2}Y_{0.2}Hf_{0.2}Zr_{0.2}O₂ nanoparticles

We synthesized Gd_{0.2}La_{0.2}Ce_{0.2}Hf_{0.2}Zr_{0.2}O₂ and

Gd_{0.2}La_{0.2}Y_{0.2}Hf_{0.2}Zr_{0.2}O₂ nanoparticles as per protocol mentioned in our previous work [27]. Predetermined amounts of individual metal salts (0.001 mol each) were dissolved together in a centrifuge tube with 30 mL deionized water (DI). Ammonia solution was added to the mixed solution to raise and maintain a pH above 12, resulting in precipitation of mixed metal hydroxides. Centrifugation was carried out to separate the precipitate from the supernatant with a speed of 12,000 rpm for 5 min. The resultant precipitate was washed with DI water until the supernatant pH was 7. Immediately after washing, DI water (5 ml) and premeditated amount of nitric acid (1:1.5 metal ion to nitric acid) was added to the wet precipitate, thoroughly mixed to break up large aggregates and the resultant suspension was sonicated (Sonics Vibra-Cell VCX 750, 750 W, 20 kHz) to get transparent sol. During the sonication, the solution temperature was not allowed to increase beyond 80 °C with an inbuilt temperature sensor, which automatically stopped the sonication when the temperature of the system reached 80 °C and started sonication when the temperature was less than 80 °C. This intermittent sonication process was continued until transparent sols were obtained. Nanopowders were obtained from the resultant sols by evaporation of solvent by drying the sols in an open container by placing in hot air oven at 110 °C for 12 h, and the obtained powders were calcined in a muffle furnace under static air at 500 °C for 4 h with a ramp of 5 °C/min to obtain Gd_{0.2}La_{0.2}Ce_{0.2}Hf_{0.2}Zr_{0.2}O₂ and Gd_{0.2}La_{0.2}Y_{0.2}Hf_{0.2}Zr_{0.2}O₂ nanoparticles and were denoted as GLCHZ-500 and GLYHZ-500 respectively.

2.2. Characterization

XRD of calcined Gd_{0.2}La_{0.2}Ce_{0.2}Hf_{0.2}Zr_{0.2}O₂ and Gd_{0.2}La_{0.2}Y_{0.2}Hf_{0.2}Zr_{0.2}O₂ nanoparticles were done using Rigaku x-ray diffractometer (Rigaku Ultima IV, Rigaku) using Cu target as a radiation source. XRD patterns were obtained using a step size of 0.02° with a scan speed of 2° per minute in the range of 20–80°. HRTEM imaging along with energy-dispersive x-ray spectra (EDS) and elemental mapping was carried out using the JEOL (JEOL JEM-2100, JEOL) and Tecnai (FEI Tecnai G2 Sphera, Tecnai) microscopes operating at an acceleration voltage of 200 kV attached with an EDS detector. For TEM analysis, powdered samples of calcined nanoparticles were dispersed in water by ultrasonication. The resultant dispersion was deposited on the carbon-coated copper grid by drop-casting and dried in air to evaporate the solvent. The surface area of the calcined photocatalysts was carried out using BET technique with the help of SMART SORB 93 (SMART SORB 93, Smart Instruments Co. Pvt. Ltd, India) instrument. UV–visible spectroscopy studies of the powdered samples were performed using the PerkinElmer LAMBDA 365 spectrophotometer in absorbance as well as reflectance mode from 200 nm to 800 nm with a step size of 1 nm. The photodegradation study was carried out using a UV–Vis Spectrophotometer (UV-1800 PC Shimadzu, Shimadzu). XPS was carried out on GLCHZ-500 and GLYHZ-500 nanoparticles using PHI 5000 Versa Prob II (FEI Inc.) instrument to obtain the O 1s spectra.

2.3. Photocatalytic reduction of toxic Cr(VI) to less toxic Cr(III)

The calcined multi-component oxides, GLCHZ-500, and GLYHZ-500 were used in the photocatalytic reduction of Cr(VI) under natural sunlight. 10 mg of potassium dichromate was dissolved in 100 mL distilled water to obtain a stock solution containing 100 ppm of potassium dichromate, which is used as a Cr(VI) source. During this experiment, a 100 ppm dichromate solution without the addition of catalyst was employed as a reference solution. The photocatalytic study was performed by taking 40 mL from 100 ppm stock solution of dichromate in a beaker, and 20 mg each of calcined multi-component oxides (GLCHZ-500 and GLYHZ-500) and 4 mL

(100%) of HCOOH was added into it. This solution was sonicated for 10 min and then kept in the dark for 10 min to establish adsorption-desorption equilibrium between the nanoparticles and Cr(VI) ions. The Cr(VI) solution with multi-component oxide nanoparticles was then irradiated under natural sunlight to ensure the reduction of Cr(VI). The reduction of the Cr(VI) into Cr(III) was monitored using a UV–Visible spectrophotometer by drawing out 3 ml aliquot from the above solution regularly at a time interval of 10 min. The complete reduction of the Cr(VI) to Cr(III) was double-checked by adding an excess of saturated NaOH associated with a formation of a green-colored precipitate ($\text{Cr}(\text{OH})_3$).

2.4. Photocatalytic degradation of methylene blue

In the same manner, the photocatalytic effectuation of GLCHZ-500 and GLYHZ-500 samples was analyzed for the degradation of methylene blue dye. The 20 mg of each calcined multi-component oxide nanoparticles were added into 40 mL of 10 ppm methylene blue solution. The mixture was then sonicated for 10 min and then kept in the dark for 10 min to reach adsorption-desorption equilibrium between nanoparticles and MB dye. Thereafter, the beaker containing the mixture was then placed under natural sunlight to test the photodegradation of methylene blue dye. 3 mL aliquot was removed from the above solution after every 15 min time interval and tested for photodegradation using a UV–Visible spectrophotometer. After the end of the first cycle, centrifugation was employed to recover the catalyst and washed with distilled water followed by methanol, and dried in hot air oven maintained at a temperature of 50 °C. The obtained catalyst was tested again to study the catalyst recyclability.

3. Results and discussions

The main objective of this study is to explore the possible applications of noble metal-free GLCHZ-500 and GLYHZ-500 multi-component oxides. In light of that, we have tried to study the photocatalytic activity of these two metal oxide systems. The phase purity of calcined nanoparticles was examined by XRD. Fig. 1 shows the x-ray diffraction patterns of GLCHZ-500 and GLYHZ-500 nanoparticles. All the reflections are indexed to (111), (200), (220), (311), (222), (400), and (331) planes of cubic fluorite structure similar to CeO_2 (ICDD PDF card number: 01-073-6318). We did not observe any additional reflections other than the reflections

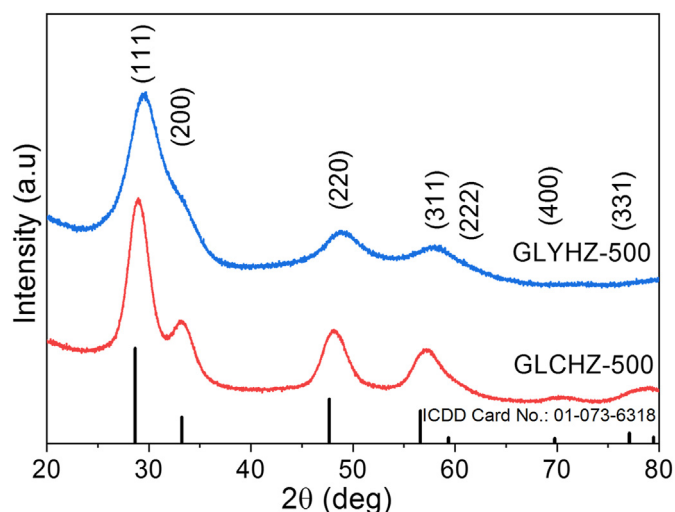


Fig. 1. Powder XRD patterns of GLCHZ-500 and GLYHZ-500 nanoparticles.

arising from the cubic fluorite structure confirming a single-phase system. A shift in reflections towards higher angles is observed compared to the standard pattern as a consequence of different sized cations present in our system. Furthermore, Rietveld refinement was performed to fit the x-ray diffraction pattern of both the GLCHZ-500 and GLYHZ-500 photocatalyst. Fig. S1 depicts the Rietveld refinement fit of the obtained photocatalyst and it confirms that the obtained x-ray diffraction fits well with the reflections of fluorite structure. Thus, we confirm that both the photocatalyst exhibit a cubic fluorite structure without any impurity phases. Williamson-Hall (W–H) method was used to calculate microstrain and average crystallite size for the synthesized powders [27]. The calculated crystallite size for GLCHZ-500 and GLYHZ-500 nanoparticles was 3.5 nm and 2.6 nm, with a microstrain of 0.29 and 0.96%, respectively. It is evident from XRD studies that the crystallite size remains small even after calcination due to large lattice strain, which is a characteristic feature of high entropy systems.

Furthermore, HRTEM was carried out to verify the presence of a single-phase cubic fluorite structure. Fig. 2 shows the HRTEM images of GLCHZ-500 and GLYHZ-500 nanoparticles. We observe the nanoparticles are in agglomerated form as a consequence of the calcination step where the nanoparticles coalesce together. We can clearly see that the nanoparticles are highly crystalline with well-defined lattice fringes, and the average particle size calculated for GLCHZ-500 and GLYHZ-500 is around 3.7 nm and 3.1 nm, respectively which is comparable to values obtained from Williamson-Hall (W–H) analysis of XRD data (Fig. S2 and Table S1).

To investigate the elemental composition as well as homogeneity in the prepared GLCHZ-500 and GLYHZ-500 photocatalysts, EDS analysis was carried out along with the elemental mapping acquired from the nanoparticle agglomerates. From Fig. S3 and Fig. S4, we confirm the presence of all the elements, and they were distributed homogeneously within the nanoparticle. Moreover, on the basis of the elemental quantification obtained from the EDS spectra (Table S2), both GLCHZ-500 and GLYHZ-500 photocatalysts

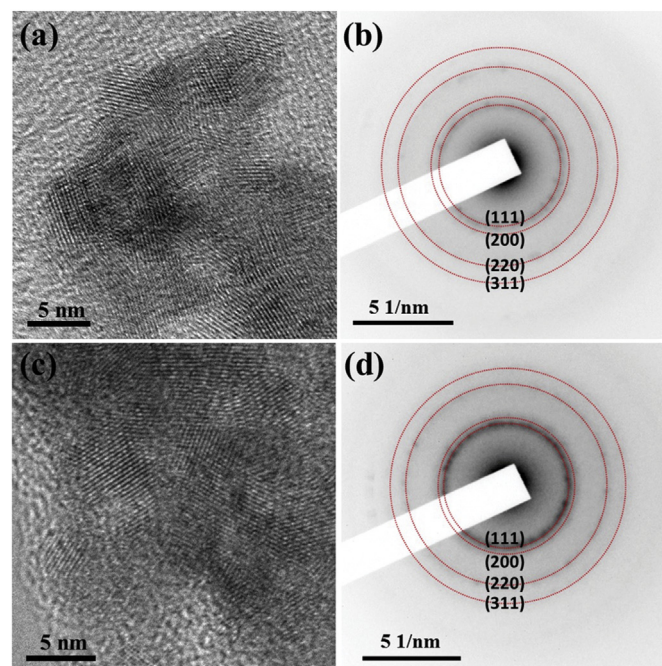


Fig. 2. TEM images (a and c) and corresponding diffraction patterns (b and d) of GLCHZ-500 (a and b) and GLYHZ-500 (c and d) nanoparticles.

contain almost equiatomic composition. Additionally, the surface area of GLCHZ-500 and GLYHZ-500 photocatalysts was carried out. The surface area for GLCHZ-500 was found to be 6.86 m²/g while for GLYHZ-500 it was 5.76 m²/g. The obtained surface area is lower than what we anticipate for nanoparticles with a particle size of roughly 3 nm. Low surface area observed for both the photocatalysts may be due to agglomeration of nanoparticles during the drying step due to lack of capping agents and further aggregation of nanoparticles during calcination step [36].

UV–visible spectroscopy was performed to study the optical properties of calcined nanoparticles, and the spectra are shown in Fig. 3. From the color variation of the nanoparticles (Fig. 3 insets) and UV–vis spectra, it is evident that though both GLCHZ-500 and GLYHZ-500 contain four identical elements and possess the same crystal structure, they show distinctly different optical behavior. This clearly indicates that the different optical behavior of these multi-component oxides is due to the synergistic interaction between individual components. This further underscores the cocktail effect observed in the case of such high entropy systems [24]. The absorption starts from 500 nm for the GLCHZ-500 sample, whereas, for the GLYHZ-500 system, absorption starts from 400 nm. The bandgap values were calculated from the reflectance spectra using the Kubelka-Munk (K-M) function $F(R)$, where $F(R) = (1-R)^2/(2R)$ and R represents the reflectance spectrum. Further, a plot between $h\nu$ versus $(F(R) \cdot h\nu)^{1/2}$ (Fig. 3 inset) was plotted and the indirect bandgap was calculated by extrapolating the term $(F(R) \cdot h\nu)^{1/2} = 0$ [37–39]. The bandgap values calculated from the Tauc plot were 2.52 eV and 3.09 eV for GLCHZ-500 and GLYHZ-500 nanoparticles.

Apart from bandgap, the positions of the valence band and the conduction band with respect to the redox potential of donor/acceptor species determine the chemical potential of photo-generated electrons and holes [40]. The potential level of acceptor species should be below the conduction band potential of the photocatalyst material, and similarly, the chemical potential of donor species should be above the valence band energy, which determines the catalyst performance [41]. Accordingly, valence band (E_{VB}) potential, as well as conduction band (E_{CB}) potential, can be calculated using the bandgap value and Mulliken electronegativity of individual cations using the following equations (1) and (2) [42].

$$E_{CB} = \chi - E^e - 0.5 E_g \quad (1)$$

$$E_{VB} = E_{CB} + E_g \quad (2)$$

where E^e is the energy of free electrons on the hydrogen scale (4.5 eV), E_g represents bandgap of the material which can be obtained from Tauc plot (2.52 eV and 3.09 eV respectively, for GLCHZ-500 and GLYHZ-500 nanoparticles) and χ represent electronegativity of oxides. For the calculation of electronegativity of overall semiconductor, the following equations were applied (3)

$$\chi = \left(\chi^A a \chi^B b \chi^C c \chi^D d \chi^E e \chi^F f \right)^{1/(a+b+c+d+e+f)} \quad (3)$$

where a, b, c, d, e, and f are the number of atoms present in the compound while A, B, C, D, E, and F are the five metal cations and one anion present in the system. The electronegativity of an individual atom can be found using (4)

$$\chi_A = \frac{1}{2} (E_{EA} + E_{IE}) \quad (4)$$

where E_{EA} and E_{IE} are electron affinity energy and ionization energy, respectively.

With the help of equations (1)–(4), the value of valence band energy (E_{VB}) and conduction band energy (E_{CB}) is estimated to be +2.355 eV and –0.164 eV versus normal hydrogen electrode (NHE) respectively for GLCHZ-500. Likewise, GLYHZ-500 has a calculated E_{VB} of +2.615 eV and E_{CB} of –0.474 eV versus NHE.

3.1. Photocatalytic reduction of Cr(VI) to Cr(III) study using noble metal-free multi-component oxides

In the present study, noble metal-free multi-component oxide nanoparticles such as GLCHZ-500 and GLYHZ-500 were used for the first time in the photoreduction of toxic Cr(VI) to less toxic Cr(III). After achieving adsorption-desorption equilibrium, natural sunlight was used as a source to reduce Cr(VI) to Cr(III), which is an added advantage since the solar spectrum covers all the energies required for photocatalysis instead of using UV or visible light. The photodegradation of Cr(VI) was monitored using UV Visible spectra with an absorption peak observed in the range of 300–420 nm, which is due to charge transfer transition of oxygen to Cr(VI).

Fig. 4a and b represent the photocatalytic performance of GLCHZ-500 and GLYHZ-500 nanoparticles, respectively towards Cr(VI) reduction. The spectral evolution of the samples was recorded at 10 min interval until complete degradation of Cr(VI) absorbance. The intensity at 350 nm peak decreases with time under exposure to natural sunlight, which indicates that Cr(VI) begins to transform to Cr(III). The complete degradation efficacy of each 0.5 mg mL⁻¹ GLCHZ-500 and GLYHZ-500 photocatalyst in 100 ppm Cr(VI) solution was observed to be 90 and 100 min on exposure to sunlight, respectively. Complete photodegradation is visually confirmed from a change in the color of the solution from yellow to colorless (Fig. 4c, i to ii). Additionally, complete reduction of the Cr(VI) to Cr(III) was confirmed by comparing the colorless solution by the addition of excess saturated NaOH solution to the reduced Cr(III) solution which results in green colored precipitates (Fig. 4c, ii to iii).

To investigate the role of multi-component oxide nanoparticle as a catalyst, we have tried the reduction of Cr(VI) in the absence of catalyst and the presence of formic acid in the dark. During this experiment, it is observed that Cr(VI) to Cr(III) reduction was not completed. This indicates that the GLCHZ-500 and GLYHZ-500 are

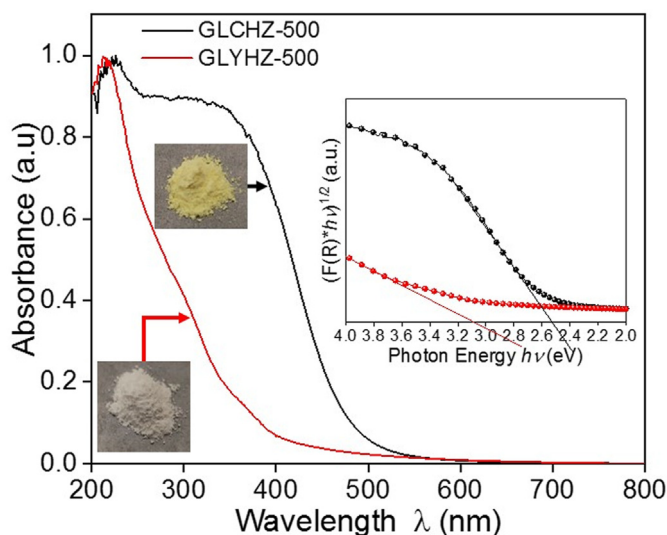


Fig. 3. UV–visible spectra of GLCHZ-500 and GLYHZ-500 nanoparticles, its visual appearance, and its corresponding bandgap plot (inset).

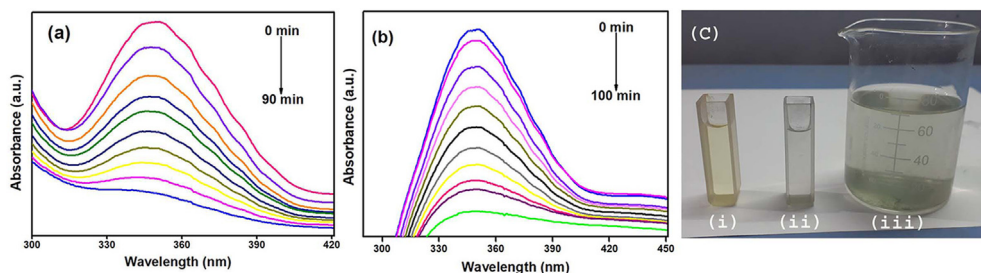


Fig. 4. UV–Visible absorption spectra for the photocatalytic reduction of Cr(VI) monitored at a time interval of 10 min during exposure to natural sunlight (a) GLCHZ-500 (b) GLYHZ-500 and (c) representative photographs of reduction of hexavalent chromium (i) Cr(VI) solution, (ii) Cr(III) solution, and (iii) after the addition of saturated NaOH solution in excess.

responsible for the reduction of Cr(VI) to Cr(III) (Fig. S5). To examine the order of reaction, a plot between the relative concentration (C_t/C_0) and irradiation time (t) was plotted (Fig. 5A) for GLCHZ-500 and GLYHZ-500 where C_0 and C_t correspond to the initial and concentration at time t . In addition to this, the plot $\ln(C_0/C_t)$ vs. time indicates pseudo-first-order kinetics (Fig. 5B).

The rate constant (k) was calculated using the Langmuir–Hinshelwood equation. The rate constant k obtained from equation $\ln(C_0/C_t) = kt$ (Fig. 5B) are 0.0175 and 0.0168 min^{-1} for GLCHZ-500 and GLYHZ-500 samples respectively.

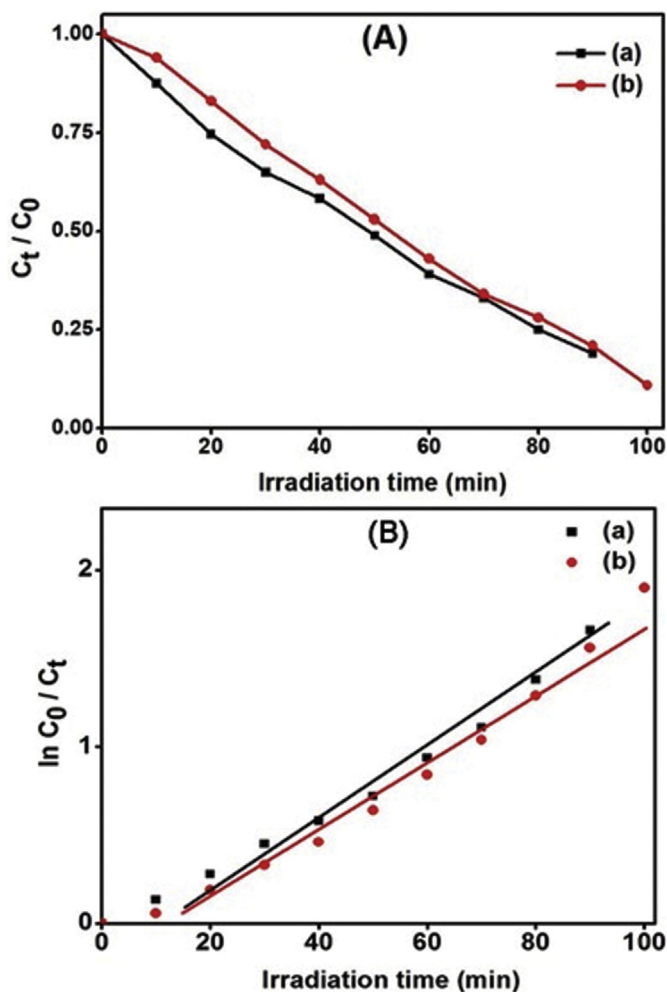


Fig. 5. (A) Plot of C_t/C_0 v/s irradiation time and (B) Plot of $\ln(C_0/C_t)$ v/s irradiation time (a) GLCHZ-500 (b) GLYHZ-500 for the degradation of Cr(VI) to Cr(III) under natural sunlight.

A significant number of literature studies demonstrate the use of a variety of metal oxides and nanocomposite materials for the reduction of the hexavalent chromium ion. The representative examples of photocatalyst with the concentrations of photocatalyst, the concentration of chromate solution, and photodegradation time are listed in Table 1. By comparing the reported results with the results obtained from our study, it is evident that both GLCHZ-500 and GLYHZ-500 show excellent photocatalytic performance for the photoreduction of Cr(VI) using natural sunlight compared to most of the reported systems. Only a few reported studies where noble metals like Pd, Pt, Ag, etc., or noble metal decorated nanocomposites have been used which showed better performance [43–45]. The most desirable aspect of the present results is that the multi-component oxide are noble metal-free and are highly efficient in terms of reduction of toxic hexavalent to less toxic trivalent chromium.

One of the objectives of our study was to correlate the optical properties of multi-component oxide systems with their photocatalytic performance. The mechanism for photocatalytic reduction of Cr(VI) to Cr(III) has been widely discussed in the literature [10,11]. Additionally, photoreduction can be elucidated by the following possible pathways.

One of the reported photoreduction mechanism is elucidated below [10]. When the surface of the nanoparticle is irradiated with sunlight, holes (h^+) and electrons (e^-) are created which stay respectively in the valence band and conduction band of oxide as denoted by equation (5)



For a nanomaterial to exhibit better photocatalytic reduction, the recombination rate of generated hole and electron should be slow. If the recombination rate is faster, then the photogenerated electrons cannot effectively engage in the reduction of Cr(VI) to Cr(III). One of the ways to decrease the recombination rate is to scavenge the available holes formed during light irradiation, which effectively leaves electrons actively involve in Cr(VI) reduction. Here, the addition of formic acid acts as a good hole scavenger that attacks holes from the valence band of oxide and forms CO_2 and H^+ as per equation (6) [46]. Thus, the addition of formic acid help in reducing the recombination rate by scavenging holes. To study the role of formic acid in Cr(VI) reduction, a control experiment without formic acid is studied and its corresponding UV Visible spectra are shown in Fig. S6. In the absence of formic acid, there is a marginal photocatalytic activity observed for both the nanoparticles which confirms the need for formic acid in the photocatalytic reduction of Cr(VI).

Table 1
Comparison of catalytic reduction of Cr(VI) with different catalyst.

| Catalyst | Amount of catalyst taken | Cr(VI) Concentration | Photoreduction time (min) | Source of light | Reference |
|---|--------------------------|----------------------|---------------------------|--|--------------|
| CQD-TiO ₂ | 1.2 mg mL ⁻¹ | 0.125 mM | 40 | Visible light | [49] |
| CDs-Silica hybrid | 1 mg mL ⁻¹ | 0.8 mM | 180 | Visible light Hg lamp | [50] |
| α-Fe ₂ O ₃ /g-C ₃ N ₄ | 1 mg mL ⁻¹ | 10 ppm | 150 | Visible light Xe lamp | [51] |
| MOF-rGO | 0.5 mg mL ⁻¹ | 10 ppm | 100 | Visible light | [52] |
| CDs-N-TiO _{2-x} | 1.0 mg mL ⁻¹ | 40 ppm | 60. | Visible light | [53] |
| CZnO-dots | 3 mg mL ⁻¹ | 100 ppm | 300 | Sunlight | [54] |
| NP-CD | 0.07 mg mL ⁻¹ | 2000 ppm | 320 | Sunlight | [55] |
| TiO ₂ (MT-1) | 1.0 mg mL ⁻¹ | 0.2 mM | 30 | UV illumination (LED light, 365 nm) | [56] |
| Fe-GCN | 0.6 mg mL ⁻¹ | 0.4 mM | 120 | Visible light Xe lamp | [57] |
| CeO ₂ -TiO ₂ | 2.0 mg mL ⁻¹ | 2 mM | 180 | Visible light Xe lamp | [58] |
| 3% Pd/CeO ₂ /g-C ₃ N ₄ | 0.5 mg mL ⁻¹ | 0.1 mM | 40 | Visible light Tungsten incandescent lamp | [59] |
| GLCHZ-500 | 0.5 mg mL ⁻¹ | 100 ppm | 90 | Sunlight | Present work |
| GLYHZ-500 | 0.5 mg mL ⁻¹ | 100 ppm | 100 | Sunlight | Present work |



Since the reduction potential of $\text{Cr}_2\text{O}_7^{2-}/\text{Cr}^{3+}$ is more positive (+1.33 eV) than the E_{CB} potential (-0.164 eV and -0.474 eV for GLCHZ-500 and GLYHZ-500 respectively), the available electrons present in the conduction band of nanoparticle reduce Cr(VI) by means of one-electron transfer. For complete Cr(VI) reduction, three electrons are consumed in order to obtain Cr(III) as per equation (7)



The reduced Cr(III) ion desorb from the nanoparticle surface paving way for the other reactive Cr(VI) ions for reduction. These overall reactions collectively reduce Cr(VI) to Cr(III) efficaciously as per equation (8), and the possible schematic of Cr(VI) detoxification is shown in Fig. 6.

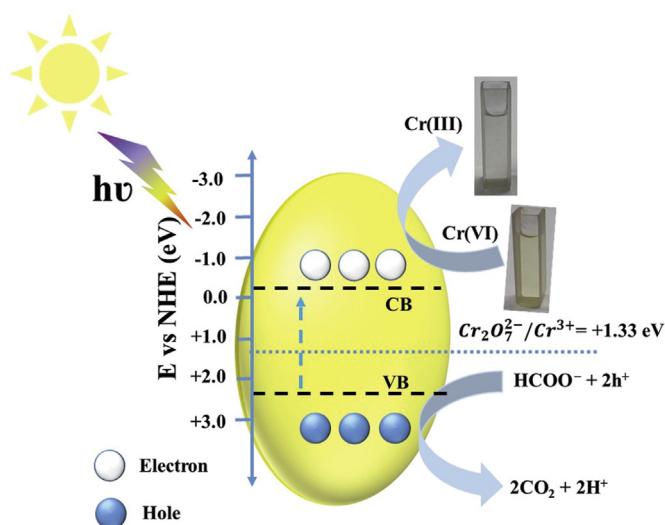


Fig. 6. Plausible mechanism of photoreduction of Cr(VI) using natural light irradiation with multi-component oxides.

Among the two compositions, GLCHZ-500 exhibited faster degradation of Cr(VI) compared to the GLYHZ-500 system. This can be a result of the bandgap narrowing of GLCHZ-500 (2.52 eV) when compared to GLYHZ-500 (3.09 eV). Lower bandgap promotes greater visible light-harvesting from natural sunlight, while less visible light interacts with the GLYHZ-500 system. Another possible explanation for enhanced degradation is the defects present in the GLYHZ-500 and GLCHZ-500 system. We believe that a large number of oxygen vacancies are present in GLYHZ-500 due to the presence of trivalent cations (Gd^{3+} , La^{3+} , Y^{3+}) in fluorite (MO_2) structure which requires tetravalent ion to maintain electro-neutrality in the structure. In the case of GLCHZ-500, in addition to Gd^{3+} and La^{3+} , cerium is also known to exist in both 3+ and 4+ oxidation states which can lead to the generation of oxygen vacancies.

To verify the presence of oxygen vacancies in the system, XPS has been carried out for both the nanoparticles. The deconvoluted O 1s core spectra for both GLCHZ-500 and GLYHZ-500 nanoparticles are shown in Fig. 7. It is observed from the spectra that four components are obtained and are labeled as O', O'', O''', and O'''. These correspond to the lattice oxygen (528.4 eV, 529.4 eV), singly charged oxygen vacancy (529.6 eV, 530.1 eV), doubly charged oxygen vacancy (531.1 eV, 531.5 eV) and hydroxyl groups (533.3 eV, 532 eV) present in the surface respectively for GLCHZ-500 and GLYHZ-500 samples [47,48]. Based on the deconvolution spectra, the oxygen stoichiometry can be calculated by using the formula

$$\text{O vacancy (\%)} = \left(\frac{A_{\text{O}'} + A_{\text{O}''}}{A_{\text{O}'} + A_{\text{O}''} + A_{\text{O}'''} + A_{\text{O}''''}} \right) / 2 * 100 \quad (9)$$

where $A_{\text{O}'}$, $A_{\text{O}''}$, $A_{\text{O}'''}$, and $A_{\text{O}''''}$ are the area under the peak O', O'', O''', and O'''' respectively. The value of oxygen stoichiometry for GLCHZ-500 is 1.66, and for the GLYHZ-500 nanoparticle, a value of 1.65 is obtained. From the XPS studies, it is evident that a large number of oxygen vacancies exist in both GLCHZ-500 and GLYHZ-500 nanoparticles. These vacancies, therefore, enhance water dissociation, which in turn facilitates Cr(VI) conversion [22].

3.2. Photocatalytic degradation of methylene blue using multi-component oxides

Considering the excellent photoreduction activity towards Cr(VI) by noble metal-free multi-component oxides, we tried to extend the photocatalytic study in wastewater treatment. Accordingly, we selected the cationic dye methylene blue as a representative for the organic pollutant. The initial concentration of MB in the solution was 10 mg L⁻¹ with a total volume of the dye solution

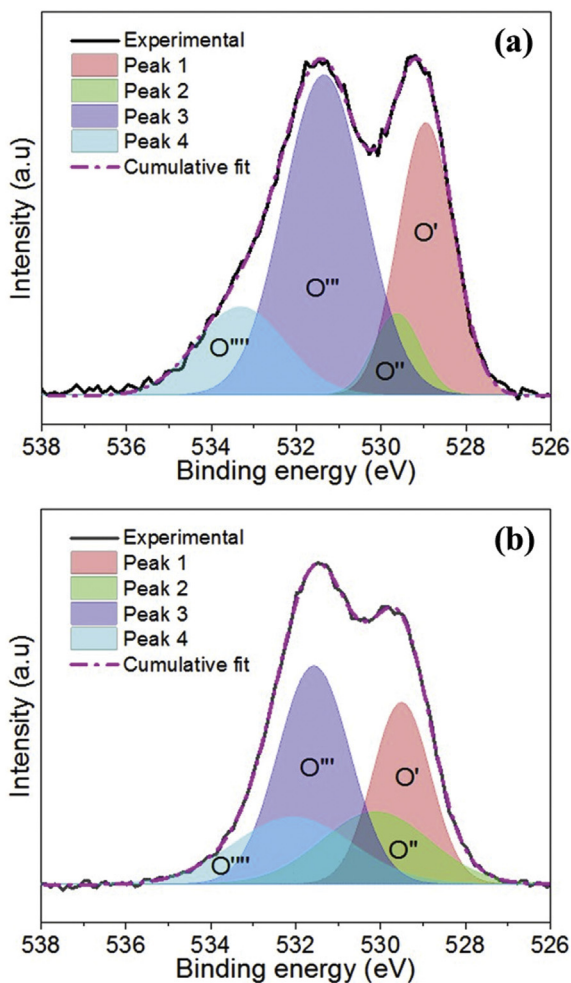


Fig. 7. Deconvoluted O 1s core level spectra of (a) GLCHZ-500 and (b) GLYHZ-500 nanoparticles.

to be 40 mL, and the catalyst dosage was 20 mg. Initially, the solution containing multi-component oxide powder and methylene blue were sonicated and kept in the dark for the accomplishment of the adsorption-desorption phenomenon.

The photocatalytic performance of GLCHZ-500 and GLYHZ-500 nanoparticles were represented in Fig. 8. The absorption spectra are recorded at every 15 min interval of time up to 180 min. Under natural sunlight, with the addition of the catalyst, the intensity at 664 nm decreases with an increase in the irradiation time. The decrease in the absorption peak at 664 nm is caused by the degradation of the benzene ring and the heteropolyaromatic linkage [60].

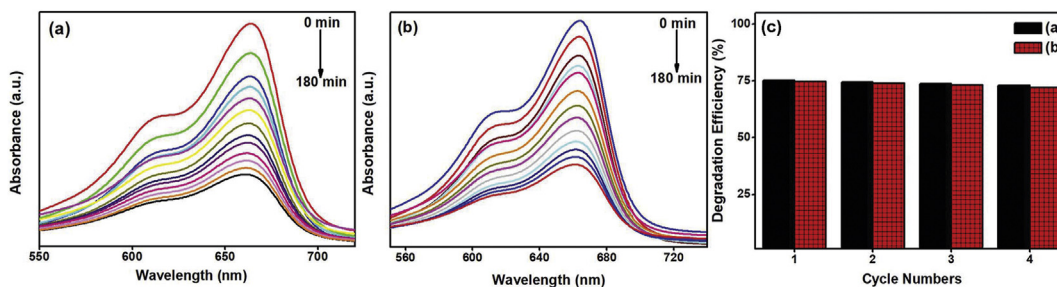


Fig. 8. UV-Vis absorption spectra of MB degradation when exposed in natural sunlight obtained at various time intervals until 180 min of (a) GLCHZ-500, (b) GLYHZ-500, and (c) recyclability test.

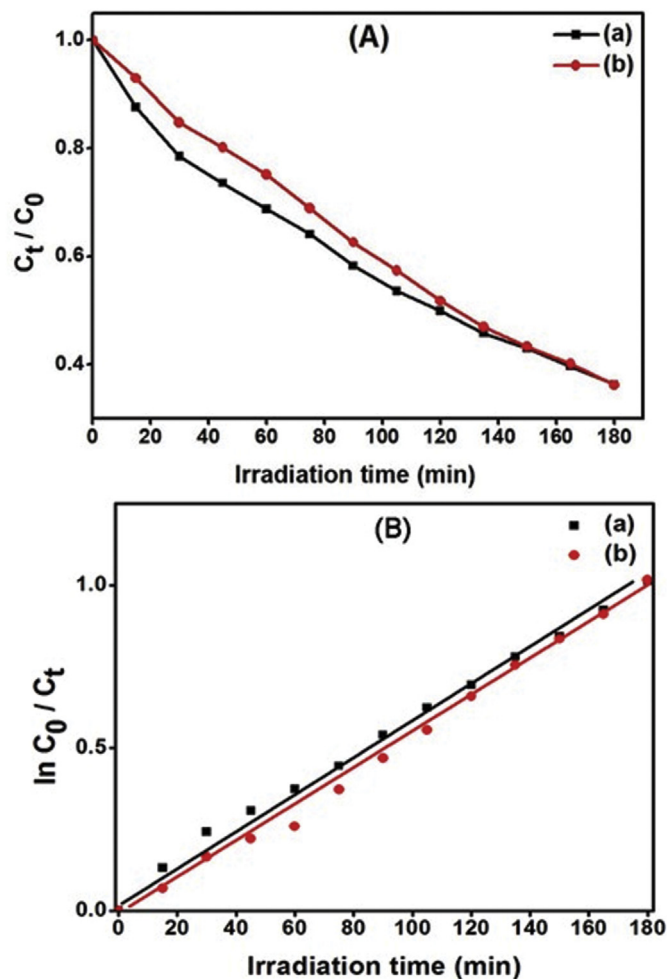


Fig. 9. (A) Plot of C_t/C_0 v/s irradiation time and (B) Plot of $\ln(C_0/C_t)$ v/s irradiation time (a) (GLCHZ-500) (b) (GLYHZ-500) for MB degradation under natural sunlight exposure at a various time interval.

Photocatalytic activity of MB has been studied using Langmuir–Hinshelwood (L–H) and modified Langmuir–Hinshelwood model. Fig. 9A shows the plot consisting of relative concentration (C_t/C_0) with irradiation time (t) to examine the order of the reaction where C_0 is the initial concentration and C_t is the concentration at time t of MB. If the concentration of the reactant is less, modified Langmuir–Hinshelwood equation is obtained *i.e.*, $\ln(C_0/C_t) = kt$, where k is the rate constant [61]. Fig. 9B shows that the plot of $\ln(C_0/C_t)$ versus solar light irradiation time t and confirm that the photocatalytic degradation of MB reaction proceeds through pseudo-first-order kinetics with respect to the

concentration of the MB. The rate constant k was found to be 0.0053 and 0.0051 min^{-1} for GLCHZ-500 and GLYHZ-500 samples respectively. Dye degradation by the catalyst was calculated by $(A_0 - A)/A_0 \times 100\%$ where A_0 and A are the absorbances of the dye at time $t = 0$ and 180 min respectively [62]. The degradation efficiency of the multi-component oxide photocatalyst was ~75.00% in both the samples. Under similar conditions, the stability of the prepared multi-component oxides was tested for recycling experiments. The observed degradation efficiency of representative GLCHZ-500 was found to be 74.02, 73.50, 73.08, and 72.60% for four consecutive cycles (Fig. 8c), which confirms better stability. In addition, to study the phase stability of the nanoparticles after photocatalytic activity, XRD of the spent catalyst was carried out which is shown in Fig. S7. It is evident that the catalyst is still stable even after multiple cycles.

4. Conclusion

The present finding briefs about the photocatalytic performance of noble metal-free multi-component equiatomic GLCHZ-500 and GLYHZ-500 nanoparticles towards wastewater treatment. Both the oxide system shows excellent photoreduction of toxic Cr(VI) to less toxic Cr(III) within 90 and 100 min, respectively, for GLCHZ-500 and GLYHZ-500 nanoparticles. Additionally, 70% degradation of the methylene blue dye was observed for both the nanoparticles within 180 min. Due to the oxygen deficiency and narrow bandgap, the obtained multi-component oxide showed absorption towards high wavelength, which further enhances the photoreduction of hexavalent chromium and MB. Formic acid helps in scavenging holes from the oxide valence band, which retards the recombination rate, thus enhancing Cr(VI) reduction. The use of noble metal-free multi-component oxides is the newer class as a photocatalyst application and most fascinating owing to its superior chemical stability, low cost, and environmental friendliness.

CRedit authorship contribution statement

Mariappan Anandkumar: Methodology, Validation, Investigation, Writing - original draft. **Ajay Lathé:** Methodology, Validation, Investigation, Writing - original draft. **Anil M. Palve:** Conceptualization, Methodology, Validation, Supervision, Writing - review & editing. **Atul Suresh Deshpande:** Conceptualization, Methodology, Validation, Supervision, Writing - review & editing.

Declaration of competing interest

The authors declare that they have no known competing financial interests or personal relationships that could have appeared to influence the work reported in this paper.

Acknowledgement

The authors are grateful to the Indian Institute of Technology for their financial and characterization support. We thank Dr. Sandesh Jaybhaye (B.K. Birla College, Kalyan, India), for carrying out surface area measurements for our samples. Anil M Palve acknowledges financial support from University of Mumbai, MRP 2018-19/593.

Appendix A. Supplementary data

Supplementary data to this article can be found online at <https://doi.org/10.1016/j.jallcom.2020.156716>.

References

[1] H.-C. Li, W.-J. Liu, H.-X. Han, H.-Q. Yu, Hydrophilic swellable metal-organic

- framework encapsulated Pd nanoparticles as an efficient catalyst for Cr(VI) reduction, *J. Mater. Chem. A*, 4 (2016) 11680–11687, <https://doi.org/10.1039/C6TA03688K>.
- [2] F.-h. Wei, D. Chen, Z. Liang, S.-q. Zhao, Y. Luo, Preparation of Fe-MOFs by microwave-assisted ball milling for reducing Cr(VI) in wastewater, *Dalton Trans.* 46 (2017) 16525–16531, <https://doi.org/10.1039/C7DT03776G>.
- [3] K. Vignesh, R. Priyanka, M. Rajarajan, A. Suganthi, Photoreduction of Cr(VI) in water using Bi₂O₃-ZrO₂ nanocomposite under visible light irradiation, *Mater. Sci. Eng., B* 178 (2013) 149–157, <https://doi.org/10.1016/j.mseb.2012.10.035>.
- [4] C.-C. Wang, X.-D. Du, J. Li, X.-X. Guo, P. Wang, J. Zhang, Photocatalytic Cr(VI) reduction in metal-organic frameworks: a mini-review, *Appl. Catal. B Environ.* 193 (2016) 198–216, <https://doi.org/10.1016/j.apcatb.2016.04.030>.
- [5] G. Jiang, Z. Lin, C. Chen, L. Zhu, Q. Chang, N. Wang, W. Wei, H. Tang, TiO₂ nanoparticles assembled on graphene oxide nanosheets with high photocatalytic activity for removal of pollutants, *Carbon* 49 (2011) 2693–2701, <https://doi.org/10.1016/j.carbon.2011.02.059>.
- [6] Q. Cheng, C. Wang, K. Doudrick, C.K. Chan, Hexavalent chromium removal using metal oxide photocatalysts, *Appl. Catal. B Environ.* 176–177 (2015) 740–748, <https://doi.org/10.1016/j.apcatb.2015.04.047>.
- [7] Q. Yuan, L. Chen, M. Xiong, J. He, S.-L. Luo, C.-T. Au, S.-F. Yin, Cu₂O/BiVO₄ heterostructures: synthesis and application in simultaneous photocatalytic oxidation of organic dyes and reduction of Cr(VI) under visible light, *Chem. Eng. J.* 255 (2014) 394–402, <https://doi.org/10.1016/j.cej.2014.06.031>.
- [8] S. Chakrabarti, B. Chaudhuri, S. Bhattacharjee, A.K. Ray, B.K. Dutta, Photoreduction of hexavalent chromium in aqueous solution in the presence of zinc oxide as semiconductor catalyst, *Chem. Eng. J.* 153 (2009) 86–93, <https://doi.org/10.1016/j.cej.2009.06.021>.
- [9] X. Liu, L. Pan, Q. Zhao, T. Lv, G. Zhu, T. Chen, T. Lu, Z. Sun, C. Sun, UV-assisted photocatalytic synthesis of ZnO-reduced graphene oxide composites with enhanced photocatalytic activity in reduction of Cr(VI), *Chem. Eng. J.* 183 (2012) 238–243, <https://doi.org/10.1016/j.cej.2011.12.068>.
- [10] A. Idris, N. Hassan, N.S. Mohd Ismail, E. Misran, N.M. Yusof, A.-F. Ngomsik, A. Bee, Photocatalytic magnetic separable beads for chromium (VI) reduction, *Water Res.* 44 (2010) 1683–1688, <https://doi.org/10.1016/j.watres.2009.11.026>.
- [11] S. Mansingh, D.K. Padhi, K.M. Parida, Enhanced visible light harnessing and oxygen vacancy promoted N, S co-doped CeO₂ nanoparticle: a challenging photocatalyst for Cr(VI) reduction, *Catal. Sci.* 7 (2017) 2772–2781, <https://doi.org/10.1039/C7CY00499K>.
- [12] S.K. Ponnaiah, P. Prakash, B. Vellaichamy, A new analytical device incorporating a nitrogen doped lanthanum metal oxide with reduced graphene oxide sheets for paracetamol sensing, *Ultrason. Sonochem.* 44 (2018) 196–203, <https://doi.org/10.1016/j.ultsonch.2018.02.016>.
- [13] Y. Wang, Y. Zhang, H. Lu, Y. Chen, Z. Liu, S. Su, Y. Xue, J. Yao, H. Zeng, Novel N-doped ZrO₂ with enhanced visible-light photocatalytic activity for hydrogen production and degradation of organic dyes, *RSC Adv.* 8 (2018) 6752–6758, <https://doi.org/10.1039/C7RA12938F>.
- [14] Z. Salehi, S. Zinatloo-Ajabshir, M. Salavati-Niasari, Dysprosium cerate nanostructures: facile synthesis, characterization, optical and photocatalytic properties, *J. Rare Earths* 35 (2017) 805–812, [https://doi.org/10.1016/S1002-0721\(17\)60980-3](https://doi.org/10.1016/S1002-0721(17)60980-3).
- [15] S. Mortazavi-Derazkola, S. Zinatloo-Ajabshir, M. Salavati-Niasari, Novel simple solvent-less preparation, characterization and degradation of the cationic dye over holmium oxide ceramic nanostructures, *Ceram. Int.* 41 (2015) 9593–9601, <https://doi.org/10.1016/j.ceramint.2015.04.021>.
- [16] M. Pirhashemi, A. Habibi-Yangjeh, S. Rahim Pouran, Review on the criteria anticipated for the fabrication of highly efficient ZnO-based visible-light-driven photocatalysts, *J. Ind. Eng. Chem.* 62 (2018) 1–25, <https://doi.org/10.1016/j.jiec.2018.01.012>.
- [17] M. Shekofteh-Gohari, A. Habibi-Yangjeh, M. Abitorabi, A. Rouhi, Magnetically separable nanocomposites based on ZnO and their applications in photocatalytic processes: a review, *Crit. Rev. Environ. Sci. Technol.* 48 (2018) 806–857, <https://doi.org/10.1080/10643389.2018.1487227>.
- [18] A. Akhundi, A. Habibi-Yangjeh, M. Abitorabi, S. Rahim Pouran, Review on photocatalytic conversion of carbon dioxide to value-added compounds and renewable fuels by graphitic carbon nitride-based photocatalysts, *Catal. Rev.* 61 (2019) 595–628, <https://doi.org/10.1080/01614940.2019.1654224>.
- [19] A. Akhundi, A. Badiei, G.M. Ziarani, A. Habibi-Yangjeh, M.J. Muñoz-Batista, R. Luque, Graphitic carbon nitride-based photocatalysts: toward efficient organic transformation for value-added chemicals production, *Molecular Catalysis* 488 (2020) 110902, <https://doi.org/10.1016/j.mcat.2020.110902>.
- [20] T. Su, Q. Shao, Z. Qin, Z. Guo, Z. Wu, Role of interfaces in two-dimensional photocatalyst for water splitting, *ACS Catal.* 8 (2018) 2253–2276, <https://doi.org/10.1021/acscatal.7b03437>.
- [21] T. Montini, M. Melchionna, M. Monai, P. Fornasiero, Fundamentals and catalytic applications of CeO₂-based materials, *Chem. Rev.* 116 (2016) 5987–6041, <https://doi.org/10.1021/acs.chemrev.5b00603>.
- [22] W.M.A. El Roubi, A.A. Farghali, A. Hamdedein, Microwave synthesis of pure and doped cerium (IV) oxide (CeO₂) nanoparticles for methylene blue degradation, *Water Sci. Technol.* 74 (2016) 2325–2336, <https://doi.org/10.2166/wst.2016.420>.
- [23] A. Mao, H.-Z. Xiang, Z.-G. Zhang, K. Kuramoto, H. Yu, S. Ran, Solution combustion synthesis and magnetic property of rock-salt (Co_{0.2}Cu_{0.2}Mg_{0.2}Ni_{0.2}Zn_{0.2})O high-entropy oxide nanocrystalline powder, *J. Magn. Magn. Mater.* 484 (2019) 245–252, <https://doi.org/10.1016/j.jmmm.2019.04.023>.

- [24] A. Sarkar, C. Loho, L. Velasco, T. Thomas, S.S. Bhattacharya, H. Hahn, R. Djenadic, Multicomponent equiatomic rare earth oxides with a narrow band gap and associated praseodymium multivalency, *Dalton Trans.* 46 (2017) 12167–12176, <https://doi.org/10.1039/C7DT02077E>.
- [25] A. Sarkar, L. Velasco, D. Wang, Q. Wang, G. Talasila, L. de Biasi, C. Kübel, T. Brezesinski, S.S. Bhattacharya, H. Hahn, B. Breitung, High entropy oxides for reversible energy storage, *Nat. Commun.* 9 (2018) 3400, <https://doi.org/10.1038/s41467-018-05774-5>.
- [26] H. Chen, J. Fu, P. Zhang, H. Peng, C.W. Abney, K. Jie, X. Liu, M. Chi, S. Dai, Entropy-stabilized metal oxide solid solutions as CO oxidation catalysts with high-temperature stability, *J. Mater. Chem. A* 6 (2018) 11129–11133, <https://doi.org/10.1039/C8TA01772G>.
- [27] M. Anandkumar, S. Bhattacharya, A.S. Deshpande, Low temperature synthesis and characterization of single phase multi-component fluorite oxide nanoparticle sols, *RSC Adv.* 9 (2019) 26825–26830, <https://doi.org/10.1039/C9RA04636D>.
- [28] M. Anandkumar, P.M. Bagul, A.S. Deshpande, Structural and luminescent properties of Eu^{3+} doped multi-principal component $\text{Ce}_{0.2}\text{Gd}_{0.2}\text{Hf}_{0.2}\text{La}_{0.2}\text{Zr}_{0.2}\text{O}_2$ nanoparticles, *J. Alloys Compd.* 838 (2020) 155595, <https://doi.org/10.1016/j.jallcom.2020.155595>.
- [29] P. Ji, J. Zhang, F. Chen, M. Anpo, Study of adsorption and degradation of acid orange 7 on the surface of CeO_2 under visible light irradiation, *Appl. Catal. B Environ.* 85 (2009) 148–154, <https://doi.org/10.1016/j.apcatb.2008.07.004>.
- [30] H. Sudrajat, S. Babel, H. Sakai, S. Takizawa, Rapid enhanced photocatalytic degradation of dyes using novel N-doped ZrO_2 , *J. Environ. Manag.* 165 (2016) 224–234, <https://doi.org/10.1016/j.jenvman.2015.09.036>.
- [31] Z. Shu, X. Jiao, D. Chen, Hydrothermal synthesis and selective photocatalytic properties of tetragonal star-like ZrO_2 nanostructures, *CrystEngComm* 15 (2013) 4288–4294, <https://doi.org/10.1039/C3CE40234G>.
- [32] H. Li, B. Feng, Visible-light-driven composite $\text{La}_2\text{O}_3/\text{TiO}_2$ nanotube arrays: synthesis and improved photocatalytic activity, *Mater. Sci. Semicond. Process.* 43 (2016) 55–59, <https://doi.org/10.1016/j.mssp.2015.11.021>.
- [33] X. Zhao, P. Wu, M. Liu, D. Lu, J. Ming, C. Li, J. Ding, Q. Yan, P. Fang, Y_2O_3 modified TiO_2 nanosheets enhanced the photocatalytic removal of 4-chlorophenol and Cr (VI) in sun light, *Appl. Surf. Sci.* 410 (2017) 134–144, <https://doi.org/10.1016/j.apsusc.2017.03.073>.
- [34] J. Ayawanna, W. Teoh, S. Niraitaisarak, K. Sato, Gadolinia-modified ceria photocatalyst for removal of lead (II) ions from aqueous solutions, *Mater. Sci. Semicond. Process.* 40 (2015) 136–139, <https://doi.org/10.1016/j.mssp.2015.06.058>.
- [35] F.N.I. Sari, S.-H. Lu, J.-M. Ting, Wide-bandgap $\text{HfO}_2\text{-V}_2\text{O}_5$ nanowires heterostructures for visible-light-driven photocatalytic degradation, *J. Am. Ceram. Soc.* (2019) 1–10, <https://doi.org/10.1111/jace.16870>.
- [36] S. Mourdikoudis, R.M. Pallares, N.T.K. Thanh, Characterization techniques for nanoparticles: comparison and complementarity upon studying nanoparticle properties, *Nanoscale* 10 (2018) 12871–12934, <https://doi.org/10.1039/C8NR02278J>.
- [37] R. López, R. Gómez, Band-gap energy estimation from diffuse reflectance measurements on sol–gel and commercial TiO_2 : a comparative study, *J. Sol. Gel Sci. Technol.* 61 (2012) 1–7, <https://doi.org/10.1007/s10971-011-2582-9>.
- [38] N. Ahmadi, A. Nemati, M. Bagherzadeh, Synthesis and properties of Ce-doped TiO_2 -reduced graphene oxide nanocomposite, *J. Alloys Compd.* 742 (2018) 986–995, <https://doi.org/10.1016/j.jallcom.2018.01.105>.
- [39] D. Palma-Ramírez, M.A. Domínguez-Crespo, A.M. Torres-Huerta, H. Dorantes-Rosales, E. Ramírez-Meneses, E. Rodríguez, Microwave-assisted hydrothermal synthesis of CePO_4 nanostructures: correlation between the structural and optical properties, *J. Alloys Compd.* 643 (2015) S209–S218, <https://doi.org/10.1016/j.jallcom.2014.12.053>.
- [40] M.D. Hernández-Alonso, F. Fresno, S. Suárez, J.M. Coronado, Development of alternative photocatalysts to TiO_2 : challenges and opportunities, *Energy Environ. Sci.* 2 (2009) 1231–1257, <https://doi.org/10.1039/B907933E>.
- [41] A.L. Linsebigler, G. Lu, J.T. Yates, Photocatalysis on TiO_2 surfaces: principles, mechanisms, and selected results, *Chem. Rev.* 95 (1995) 735–758, <https://doi.org/10.1021/cr00035a013>.
- [42] M. Mousavi, A. Habibi-Yangjeh, M. Abitorabi, Fabrication of novel magnetically separable nanocomposites using graphitic carbon nitride, silver phosphate and silver chloride and their applications in photocatalytic removal of different pollutants using visible-light irradiation, *J. Colloid Interface Sci.* 480 (2016) 218–231, <https://doi.org/10.1016/j.jcis.2016.07.021>.
- [43] S. Li, J. Cai, X. Wu, B. Liu, Q. Chen, Y. Li, F. Zheng, $\text{TiO}_2/\text{Pt}/\text{CeO}_2$ nanocomposite as a bifunctional catalyst for enhancing photo-reduction of Cr (VI) and photo-oxidation of benzyl alcohol, *J. Hazard Mater.* 346 (2018) 52–61, <https://doi.org/10.1016/j.jhazmat.2017.12.001>.
- [44] S. Patnaik, D. Prava Sahoo, K.M. Parida, Bimetallic co-effect of Au-Pd alloyed nanoparticles on mesoporous silica modified $g\text{-C}_3\text{N}_4$ for single and simultaneous photocatalytic oxidation of phenol and reduction of hexavalent chromium, *J. Colloid Interface Sci.* (2019), <https://doi.org/10.1016/j.jcis.2019.09.041>.
- [45] R.A. Badhe, A. Ansari, S.S. Garje, One-pot synthesis of Pd-based ternary Pd@CdS/ TiO_2 nanoclusters via a solvothermal route and their catalytic reduction efficiency toward toxic hexavalent chromium, *ACS Omega* 3 (2018) 18663–18672, <https://doi.org/10.1021/acsomega.8b02924>.
- [46] S. Zheng, Y. Cai, K.E. O'Shea, TiO_2 photocatalytic degradation of phenylarsonic acid, *J. Photochem. Photobiol., A* 210 (2010) 61–68, <https://doi.org/10.1016/j.jphotochem.2009.12.004>.
- [47] L. Zhao, J. Zhao, T. Wu, M. Zhao, W. Yan, Y. Zhang, H. Li, Y. Wang, T. Xiao, Y. Zhao, Synergistic effect of oxygen vacancies and Ni species on tuning selectivity of Ni/ ZrO_2 catalyst for hydrogenation of maleic anhydride into succinic anhydride and γ -butyrolactone, *Nanomaterials* 9 (2019) 406, <https://doi.org/10.3390/nano9030406>.
- [48] R. Jain, A. Dubey, M.K. Ghosal, C.S. Gopinath, Gas–solid interaction of $\text{H}_2\text{-Ce}_{0.95}\text{Zr}_{0.05}\text{O}_2$: new insights into surface participation in heterogeneous catalysis, *Catal. Sci.* 6 (2016) 1746–1756, <https://doi.org/10.1039/C5CY01428J>.
- [49] D. Choi, S. Ham, D.-J. Jang, Visible-light photocatalytic reduction of Cr(VI) via carbon quantum dots-decorated TiO_2 nanocomposites, *J. Environ. Chem. Eng.* 6 (2018) 1–8, <https://doi.org/10.1016/j.jece.2017.11.065>.
- [50] Y. Liu, Y.-j. Ma, C.-y. Liu, Z.-y. Zhang, W.-d. Yang, S.-d. Nie, X.-h. Zhou, The effective removal of Cr(VI) ions by carbon dot–silica hybrids driven by visible light, *RSC Adv.* 6 (2016) 68530–68537, <https://doi.org/10.1039/C6RA13593E>.
- [51] D. Xiao, K. Dai, Y. Qu, Y. Yin, H. Chen, Hydrothermal synthesis of $\alpha\text{-Fe}_2\text{O}_3/g\text{-C}_3\text{N}_4$ composite and its efficient photocatalytic reduction of Cr(VI) under visible light, *Appl. Surf. Sci.* 358 (2015) 181–187, <https://doi.org/10.1016/j.apsusc.2015.09.042>.
- [52] L. Shen, L. Huang, S. Liang, R. Liang, N. Qin, L. Wu, Electrostatically derived self-assembly of NH_2 -mediated zirconium MOFs with graphene for photocatalytic reduction of Cr(VI), *RSC Adv.* 4 (2014) 2546–2549, <https://doi.org/10.1039/C3RA45848B>.
- [53] L. Xu, X. Bai, L. Guo, S. Yang, P. Jin, L. Yang, Facial fabrication of carbon quantum dots (CDs)-modified N- TiO_2 -x nanocomposite for the efficient photoreduction of Cr(VI) under visible light, *Chem. Eng. J.* 357 (2019) 473–486, <https://doi.org/10.1016/j.cej.2018.09.172>.
- [54] P. Khare, A. Bhati, S.R. Anand, Gunture, S.K. Sonkar, Brightly fluorescent zinc-doped red-emitting carbon dots for the sunlight-induced photoreduction of Cr(VI) to Cr(III), *ACS Omega* 3 (2018) 5187–5194, <https://doi.org/10.1021/acsomega.8b00047>.
- [55] A. Bhati, S.R. Anand, D. Saini, Gunture, S.K. Sonkar, Sunlight-induced photoreduction of Cr(VI) to Cr(III) in wastewater by nitrogen-phosphorus-doped carbon dots, *npj Clean Water* 2 (2019) 12, <https://doi.org/10.1038/s41545-019-0036-z>.
- [56] Y. Li, Y. Bian, H. Qin, Y. Zhang, Z. Bian, Photocatalytic reduction behavior of hexavalent chromium on hydroxyl modified titanium dioxide, *Appl. Catal. B Environ.* 206 (2017) 293–299, <https://doi.org/10.1016/j.apcatb.2017.01.044>.
- [57] X. Wang, M. Hong, F. Zhang, Z. Zhuang, Y. Yu, Recyclable nanoscale zero valent iron doped $g\text{-C}_3\text{N}_4/\text{MoS}_2$ for efficient photocatalysis of RhB and Cr(VI) driven by visible light, *ACS Sustain. Chem. Eng.* 4 (2016) 4055–4063, <https://doi.org/10.1021/acssuschemeng.6b01024>.
- [58] H. Jiang, M. Li, J. Liu, X. Li, L. Tian, P. Chen, Alkali-free synthesis of a novel heterostructured $\text{CeO}_2\text{-TiO}_2$ nanocomposite with high performance to reduce Cr(VI) under visible light, *Ceram. Int.* 44 (2018) 2709–2717, <https://doi.org/10.1016/j.ceramint.2017.10.225>.
- [59] K. Saravanakumar, R. Karthik, S.-M. Chen, J. Vinoth Kumar, K. Prakash, V. Muthuraj, Construction of novel Pd/ $\text{CeO}_2/g\text{-C}_3\text{N}_4$ nanocomposites as efficient visible-light photocatalysts for hexavalent chromium detoxification, *J. Colloid Interface Sci.* 504 (2017) 514–526, <https://doi.org/10.1016/j.jcis.2017.06.003>.
- [60] J. Lin, Z. Luo, J. Liu, P. Li, Photocatalytic degradation of methylene blue in aqueous solution by using ZnO-SnO_2 nanocomposites, *Mater. Sci. Semicond. Process.* 87 (2018) 24–31, <https://doi.org/10.1016/j.mssp.2018.07.003>.
- [61] S. Kandula, P. Jeevanandam, Sun-light-driven photocatalytic activity by ZnO/Ag heterostructures synthesized via a facile thermal decomposition approach, *RSC Adv.* 5 (2015) 76150–76159, <https://doi.org/10.1039/C5RA14179F>.
- [62] N. Neelakandeswari, G. Sangami, N. Dharmaraj, N.K. Taek, H.Y. Kim, Spectroscopic investigations on the photodegradation of toluidine blue dye using cadmium sulphide nanoparticles prepared by a novel method, *Spectrochim. Acta, Part A* 78 (2011) 1592–1598, <https://doi.org/10.1016/j.saa.2011.02.008>.